AGU PUBLICATIONS

JGR

Journal of Geophysical Research: Space Physics

TECHNICAL REPORTS: METHODS

10.1002/2016JA022911

Key Points:
- Method of magnetotail magnetic flux calculation based on two spacecraft observations in the near or middle tail and solar wind is presented
- It was tested and calibrated on global MHD and empirical T14 models as well as on polar cap observations and Cluster and THEMIS measurements
- The proposed algorithm is able to estimate the magnetotail magnetic fluxvalue and dynamics in real-time and retrospective regimes

Supporting Information:
- Supporting Information S1
- Table S1

Correspondence to:
M. A. Shukhtina,
mshukht@geo.phys.spbu.ru;
m.shuhtina@spbu.ru

Citation:
Shukhtina, M. A., E. I. Gordeev, V. A. Sergeev, N. A. Tsyganenko, L. B. N. Clausen, and S. E. Milan (2016), Magnetotail magnetic flux monitoring based on simultaneous solar wind and magnetotail observations, *J. Geophys. Res. Space Physics*, *121*, 8821–8839, doi:10.1002/2016JA022911.

Received 6 MAY 2016
Accepted 19 AUG 2016
Accepted article online 23 AUG 2016
Published online 17 SEP 2016

Magnetotail magnetic flux monitoring based on simultaneous solar wind and magnetotail observations

M. A. Shukhtina[1], E. I. Gordeev[1], V. A. Sergeev[1], N. A. Tsyganenko[1], L. B. N. Clausen[2], and S. E. Milan[3,4]

[1]Department of Earth's Physics, Saint Petersburg State University, Saint Petersburg, Russia, [2]Department of Physics, Oslo, Norway, [3]Birkeland Centre for Space Science, University of Bergen, Bergen, Norway, [4]Department of Physics and Astronomy, University of Leicester, Leicester, UK

Abstract The magnetotail magnetic flux (MTF) is an important global variable to describe the magnetospheric state and dynamics. Existing methods of MTF estimation on the basis of the polar cap area, inferred from observations of global auroras and field-aligned currents, do not allow benchmarking due to the absence of a gauge for comparison; besides, they rarely allow a systematic nearly real time MTF monitoring. We describe three modifications (F_0, F_1, and F_2) of the method to calculate the MTF, based on simultaneous spacecraft observations in the magnetotail and in the solar wind, suitable for real-time MTF monitoring. The MTF dependence on the solar wind parameters and the observed tail lobe magnetic field is derived from the pressure balance conditions. An essential part of this study is the calibration of our approximate method against global 3-D MHD simulations and the empirical T14 magnetospheric field model. The calibration procedure provides all variables required to evaluate F_0, F_1, and F_2 quantities and, at the same time, computes the reference MTF value through any tail cross section. It allowed us to extend the method to be used in the near tail, investigate its errors, and define the applicability domain. The method was applied to Cluster and THEMIS measurements and compared with methods of polar cap area calculation based on IMAGE and AMPERE observations. We also discuss possible applications and some recent results based on the proposed method.

1. Introduction

The open magnetotail flux (MTF) is an important global magnetospheric state variable describing the global magnetotail equilibrium; its value controls the tail flaring rate and the transverse dimension of the magnetosphere as well as the auroral oval and polar cap size [*Coroniti and Kennel*, 1972]. It also plays an important role in quantifying the dynamical reconfigurations of the magnetotail during disturbances [*Fairfield*, 1985]. The basic concept of the magnetospheric dynamics is the magnetic flux circulation scheme, proposed by *Dungey* [1961] and further developed by *Russell and McPherron* [1973], *Siscoe and Huang* [1985], *Cowley and Lockwood* [1992], and others. According to that concept, different magnetospheric states result from the imbalance between the dayside and nightside reconnection rates. In particular, during the substorm growth phase the dayside reconnection rate is much larger than the nightside one, which results in accumulation of the MTF. The net MTF increase by the end of that phase corresponds to the amount of the magnetic flux that may be potentially reconnected during the substorm expansion phase, when the nightside reconnection rate abruptly increases and exceeds the intake rate on the dayside, resulting in the MTF reduction. An alternative magnetospheric state is the stationary magnetospheric convection (SMC) [*Sergeev et al.*, 1996], characterized by the balance between the dayside and nightside reconnection rates, as implied by its substitute name, the Balanced Reconnection Intervals [*DeJong et al.*, 2008].

Despite being a key global variable to characterize the static and dynamic states of the magnetospheric system, the MTF is hard to derive and monitor on the basis of local ground or space observations, so that only scarce quantitative information on the MTF and its variations has been available for a long time. *Mishin* [1990] proposed Magnetic Inversion Technique which used the polar cap evaluated based on high-latitude magnetometer network observations to calculate the MTF value. However, as this method has not been calibrated against independent magnetic flux estimates, its accuracy is not known, and it will not be discussed here.

The situation seemed to change two decades ago, when the global auroral images of Polar and Imager for Magnetopause-to-Aurora Global Exploration (IMAGE) spacecraft became available [*Brittnacher et al.*, 1999; *Milan et al.*, 2003; *DeJong and Clauer*, 2005; *Hubert et al.*, 2006]. Based on those images, the polar cap (PC) area and magnetic flux (FPC) can be calculated. A common belief is that the open (lobe) magnetic flux threads the polar caps, and hence, the FPC provides a measure of the MTF [e.g., *Milan et al.*, 2003]. However, unambiguous identification of the polar cap boundary has its own problems. It suffers from the dayglow contamination and from low precipitated energy flux (resulting in low auroral luminosity, close to the detection threshold) near the PC boundary. The dayglow problem is not that important if using the proton Doppler-shifted auroral Lyman-alpha emission observed by IMAGE SI12 imager [*Hubert et al.*, 2006], whereas the instrumentation sensitivity is a more serious issue. Another problem of those methods is the limited data coverage since no global auroral images are available after 2008, during the time period covered by Time History of Events and Macroscale Interactions during Substorms (THEMIS), Van Allen Probes, and Magnetospheric Multiscale (MMS) missions.

Recently, the Active Magnetospheric and Planetary Electrodynamics Response Experiment (AMPERE) [*Anderson et al.*, 2000, 2002] has made it possible to estimate the PC area and the FPC value by observing global distributions of the field-aligned currents (FACs). Since the region 1 current oval has been shown to statistically collocate with the open/closed field line boundary, obtained from Defense Meteorological Satellite Program (DMSP) particle measurements [*Clausen et al.*, 2013], we can estimate FPC by automatically finding the region 1 current oval as described in *Clausen et al.* [2012] and then integrating the magnetic flux bounded by this contour. This method has its own limitations. During periods of low solar wind driving, the large-scale region 1 and region 2 currents are no longer detectable by AMPERE such that the automatic R1 oval determination fails. During more active times, however, the region 1/region 2 currents are well defined, and the analysis can be done. The accuracy of this method is a more difficult question, primarily because of the sampling rate and corresponding spatial resolution of original IRIDIUM records (the nominal resolution is 1° latitude and 2 h MLT for the *B* field measurements). According to the authors' experience, in a statistical sense the region 1 oval detection is accurate to about 1° magnetic latitude, whereas in individual cases the difference can be larger. Note here that at typical auroral latitudes, the 1° uncertainty translates into an FPC error as high as ~10%. As for the methods based on the observations of global auroras, it should be noted that different instruments give different results (up to ±2° of polar cap boundary latitude in some sectors), and their deviation from the DMSP particle boundaries also varies [*Boakes et al.*, 2008].

Also, there exists another essential and difficult problem, not widely known. Namely, the mapping of the open/closed field line boundary (reconnection separatrix) from the distant tail to the low-altitude PC boundary is actually violated as these field lines are transported across the reconnection separatrix. Here the reconnection-accelerated particles moving along the field lines are convected inward across the separatrix during their flight to the ionosphere, and therefore, their precipitation locations are shifted equatorward from the separatrix foot point. This effect has been reported to take place during solar particle events, when the detected poleward precipitation boundary is shifted equatorward from the separatrix by as much as 1–3° of latitude [*Sergeev and Bösinger*, 1993], with the observed shift extending over azimuthal sectors as wide as 5 h of MLT [*Zhang et al.*, 2011]. This may cause a systematic mismatch between the FPC and MTF values up to 10–20% during some episodes of high magnetospheric activity and unbalanced reconnection rate.

The recent study of *Carter et al.* [2016] performed an indirect comparison of FACs position, given by AMPERE, with auroral UV emissions, observed by IMAGE. This study (unexpectedly) revealed a discrepancy between the region 1 current location and auroral oval in the dusk sector. Summarizing, the results obtained from the polar cap observations should be considered with caution (and need additional validation).

MTF variations are associated with the tail lobe magnetic field variations and changes of the lobes' size. *Petrinec and Russell* [1996, hereafter PR96] proposed an empirical axisymmetric magnetopause model and used it to compute the MTF based on the directly measured lobe magnetic field (B_L). In *Shukhtina et al.* [2009] we developed the PR96 approach such that the magnetopause radius and the corresponding MTF value F_0 are computed using magnetotail and solar wind measurements for each particular time. In *Shukhtina and Gordeev* [2015, hereafter SG'15] two modifications of the method, F_1 and F_2, suitable in the inner

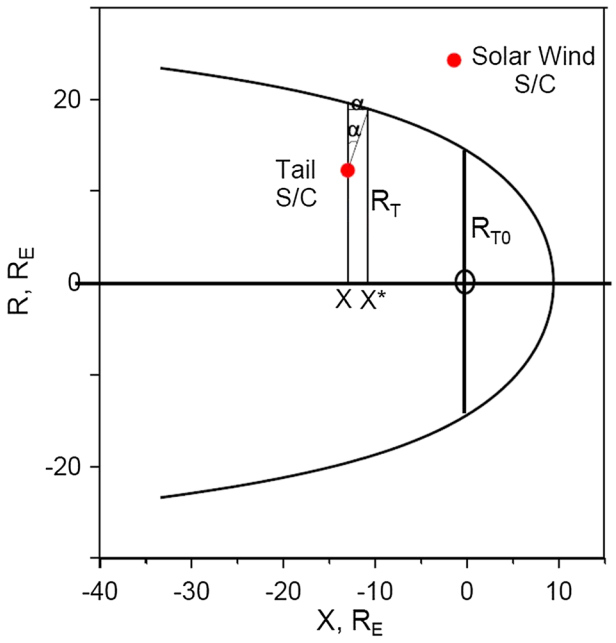

Figure 1. The scheme illustrating the procedure of magnetotail radius calculation.

magnetosphere, were introduced. In section 2 we overview all three estimates, after which we present their calibration and validation (the main goal of this paper).

2. Magnetotail Magnetic Flux Calculation

2.1. F_0 Algorithm (Assumes Tail Approximation)

If a spacecraft observes the field B_L near the tail boundary, its radius can be obtained from the pressure balance at the flaring magnetopause (α for the flaring angle):

$$0.88\,Pd\,\sin^2\alpha + B_{sw}^2/2\mu_0 + n_{sw}\,kT_{sw} = B_L^2/2\mu_0 \quad (1)$$

where the left-hand side variables refer to the upstream solar wind: the dynamic pressure Pd, the interplanetary magnetic field B_{sw}, ion density n_{sw}, and temperature $T_{sw} = T_{isw} + T_{esw}$, while the right-hand side term is the tail lobe magnetic pressure. The coefficient 0.88 is the theoretical value of the ratio of the stagnation point pressure to the ram pressure in the upstream solar wind beyond the bow shock for high Mach numbers [*Spreiter et al.*, 1966]. (Note that PR96 ignored the difference between the solar wind and the stagnation point pressure and used the coefficient 1 instead of 0.88; though it does not crucially change the result, we suppose the value 0.88 is more accurate, and use equation (1) everywhere.) If the magnetotail spacecraft is located in the plasma sheet rather than in the lobes, the equivalent lobe field B_L can be determined from the observed magnetic field and plasma parameters by assuming the one-dimensional pressure balance in the tail:

$$B_L^2/2\mu_0 = B^2/2\mu_0 + nkT. \quad (2)$$

When the α value is determined from (1), it is possible to calculate the tail radius R_T at distance X as

$$R_T = R_{T0} + \int_0^X \tan\alpha\,dx — \quad (3)$$

see Figure 1 (here R_{T0} is the tail radius value at the terminator (at $X = 0$)). Based on a large data set of simultaneous solar wind and tail lobe measurements, PR96 carried out a multifactor analysis of $\sin^2\alpha$ as a function of the solar wind dynamic pressure Pd, IMF B_z, and X coordinate in the tail to construct the statistical shape of the magnetopause as $R_T(X, Pd,$ and$IMF\ B_z)$.

For a more general case of the magnetotail spacecraft being located at a finite distance from the boundary, PR96 suggested a method to project the spacecraft location to the magnetopause, i.e., to find a magnetopause point with $X_{GSM} = X^*$ (Figure 1) where the magnetic field has the same magnitude B_L as measured by the spacecraft inside the lobe at $X_{GSM} = X$. They noticed that in the flaring part of the tail the lobe field lines are nearly parallel to the boundary, and the contours $B_L =$ const are nearly perpendicular to magnetopause. Thus, the desired X coordinate equals $X^* = X + \Delta X$, where $\Delta X = \left(R_T - \left(Y^2 + Z^2\right)^{1/2}\right)\sin\alpha\cos\alpha$. PR96 used an iterative procedure, in which at the first step the X^* values for the entire data set were calculated from $\sin^2\alpha(X)$ shape, obtained from (1); at the second iteration the updated dependence $\sin^2\alpha(X^*)$, and the new X^* were found, and so on. The procedure was found to quickly converge, such that after several iterations the tail radius was determined.

Using the above procedure, PR96 constructed an empirical magnetopause model, driven by the interplanetary magnetic field (IMF)/solar wind parameters and the X coordinate. The model was based on observations

of ISEE2 spacecraft with X between −10 and −22 R_E, IMF B_Z in the range (−10 nT and +10 nT), and P_d within (0.5 nPa and 8 nPa).

Note, however, that the shape of the magnetotail boundary depends not only on the solar wind parameters, but it may also be different for different magnetospheric states (for example, at the beginning and at the end of the growth phase [e.g., *Maezawa*, 1975]. To show this, *Shukhtina et al.* [2004] carried out a similar statistical study to obtain the model in the form $\sin^2\alpha(X, P_d, <E_m>) = \sin^2\alpha(X)\cdot\sin^2\alpha(P_d)\cdot\sin^2\alpha(<Em>)$ (where $<E_m> = <V_{sw}\left(B_{ysw}^2 + B_{zsw}^2\right)^{1/2}\sin^3\theta/2>$ is the "merging" electric field, averaged over 1 h, preceding the observation moment and θ is the IMF clock angle) but did it separately for different magnetospheric states (quiet, substorm onset, SMC). Following PR96, the $\sin^2\alpha(X)$ dependence was taken as $\sin^2\alpha(X) \sim \exp(CX)$. While the models were found to yield significantly different results for different states (mainly due to $\alpha(E_m)$ dependence), the obtained C values were quite similar, with the average $C = 0.0714$. Bearing that in mind, *Shukhtina et al.* [2009] proposed a modification of the PR96 method, in which the α value was not taken from the statistical model but was calculated at each time step based on in situ-measured lobe field values. Assuming $\sin^2\alpha = A^2\exp(CX)$ with $C = 0.0714$, the variable A is uniquely determined from (1), and the integration of (3) gives

$$R_T(X^*) = R_{T0} - 2/C(\arcsin(A^*\exp(CX^*/2)) - \arcsin(A^*)), \tag{4}$$

where A^* is obtained as a result of several iterations.

At this stage using the "measured" lobe field B_L and in situ calculated tail radius value R_T, the tail magnetic flux (F_0) through the half of circular tail cross section can be estimated as

$$F_0 = 0.5\pi R_T^2 B_L, \tag{5}$$

assuming B_L to be approximately constant over the particular magnetotail cross section.

Equations (1)–(5) provide the basics of the MTF calculation based on in situ spacecraft measurements in the magnetotail complemented by the simultaneous properly time-shifted observations in the solar wind. In this form the algorithm includes a number of strong assumptions (A1 to A6) which have to be explicitly mentioned and shortly commented.

(A1) Zero dipole tilt. The zero tilt is assumed from the outset in the algorithm, as geometrically illustrated in Figure 1. This restriction is not critical for the middle tail beyond 10–15 R_E, since the neutral sheet is aligned approximately parallel to the solar wind tailward from the "hinging distance" of ~10 R_E [*Tsyganenko and Fairfield*, 2004]. However, at closer distances the entire configuration becomes strongly deformed, such that significant errors should be expected for large tilt angles.

(A2) Magnetopause radius at terminator. The magnetopause position in the $X = 0$ cross section (R_{T0}) serves as the boundary condition for integrating equation (3), so that its accuracy affects the accuracy of the MTF estimate. Initially, we used the formula from PR96: $R_{T0} = 14.63(Pd/2.1)^{1/6}$ which does not include any IMF dependence. In SG'15 the formula for R_{T0} was reexamined based on magnetopause crossings' data set for 1963–1998 from the NASA GSFC website (http://ftpbrowser.gsfc.nasa.gov/magnetopause.html). Together with the dependence on the dipole tilt angle Ψ and Pd, that analysis revealed a clear (though modest) dependence on the IMF B_z hourly values:

$$R_{T0} = (14.1 + 0.045\Psi)1.161\,Pd^{1/6.02}(1.004 - 0.0054\,\mathrm{IMF}\,B_z), \tag{6}$$

providing a better correlation with the original data ($CC = 0.74$, std = 1.07 R_E) compared to the PR96 one ($CC = 0.54$, std = 1.27 R_E). In comparison with global 3-D MHD (GMHD) simulations in sections 3.1 and 3.2 (with $\Psi = 0$, according to the assumption A1) the equation (6) is reduced to

$$R_{T0} = 16.37\,Pd^{1/6.02}(1.004 - 0.0054\,\mathrm{IMF}\,B_z). \tag{6a}$$

(A3) Axial symmetry of the magnetopause and neglecting the finite width of the plasma sheet. According to the recent models, the midtail magnetopause ellipticity (for zero dipole tilt, assumption A1) is small and may be ignored. For example, according to *Lin et al.* [2010] at $X = -15$ R_E the ratio of the dawn/dusk to north/south magnetopause radii equals $\Delta Y/\Delta Z = 1.04$ for Pd=3 nPa and IMF B_z in the range (−10 nT and +10 nT).

The plasma sheet thickness Δ is a strongly variable parameter both in time and space. Its statistical study became possible due to Cluster multispacecraft observations [e.g., *Thompson et al.*, 2005; *Petrukovich et al.*, 2007, 2011; *Rong et al.*, 2011]; another way to estimate Δ is to use observations of the current sheet flapping motion [*Sergeev et al.*, 1998, 2003; *Runov et al.*, 2005; *Artemyev et al.*, 2015]. These studies as well as few earlier researches give the approximate plasma sheet thickness at geocentric distances 13–19 R_E between 0.5 and 5 R_E [*Panov et al.*, 2010, and references therein]. For $X = -13(-19)$ R_E, $Pd = 3$ nPa, IMF $B_z = -5$ nT, the *Lin et al.* [2010] model gives R_T=20(22) R_E. The ratio of the plasma sheet cross-tail area ($2R_T^*\Delta$) to the total cross-tail area (πR_T^2), equal to $2\Delta/\pi R_T$, can reach ~15% in the midtail. Note that the latter value may considerably change in the course of substorms [*Baumjohann et al.*, 1992; *Sergeev et al.*, 1993; *Dewhurst et al.*, 2004; *Petrukovich et al.*, 2011] and during a bursty bulk flow (BBF) passage [*Panov et al.*, 2010].

In view of the above caveats, the algorithm (1)–(5) gives an upper estimate of the total magnetic flux through the given tail cross section. Neglecting the finite width of plasma sheet, where the magnetic field lines are closed and the magnetic field magnitude is lower than in the lobes, is unavoidable at the moment. That point will be discussed below in section 3.2 in relation to the model calibration.

(A4) Nonuniform lobe field and projecting spacecraft locations to the magnetopause. According to one of our main presumptions, the contours of equal lobe field B_L intersect the flaring magnetopause at right angles, and hence, B_L values are different at locations with the same X but different Z. Note that the PR96 model was based on ISEE 2 data taken at high latitudes, where the B_L contours are indeed nearly perpendicular to the magnetopause. At lower latitudes, however, the lobe magnetic field lines are nearly parallel to the neutral sheet, and hence, the B_L isolines are oriented in the Z direction there. Therefore, in the meridional section $Y = 0$ the equal pressure contours have nearly circular shape, being parallel to Z axis at low latitudes and perpendicular to the magnetopause near the boundary. However, in our algorithm we consider the equal B_L contours to be everywhere perpendicular to the magnetopause. This assumption overestimates the value of the "correction" ΔX of the X coordinate for observations in the plasma sheet (Figure 1) but is reasonable for the tail lobe observations (which are mainly used in the present paper).

(A5) Tail approximation and dipole field contribution. This point is related to (A4) and has two important aspects. The first aspect is that the tail pressure balance (2) implies a nearly one-dimensional configuration in which the field-aligned Maxwell tension is negligible compared to the pressure gradient terms. This requirement is always violated in the near tail, but it can also break down in the middle and far magnetotail during the episodes of flow burst and plasmoid activities. The second aspect is that a nonnegligible part of the lobe field in the near tail (at $r < 10 - 15$ R_E) is provided by the dipole field, which does not contribute to our target quantity, the open magnetotail magnetic flux.

These difficulties may be partly avoided by applying the method only in the nominal region of the tail approximation validity (tailward 15–20 R_E), but it means a loss of a considerable amount of potentially useful observations in the near tail made by spacecraft on highly eccentric orbits (like Cluster, innermost THEMIS spacecraft, etc). Besides, in this region the most strong variations of the tail currents develop, and most observations are made. Therefore, a possibility to extend applicability of MTF estimates from observations, made in the near tail, is a challenging practical task. This problem is discussed in section 2.2.

(A6) Time-delay problems in the strongly variable solar wind. Sharp and significant variation of solar wind parameters are incompatible with the quasi-static balance assumption implied by equation (1). This is a strong natural constraint in the practical implementation of the method. A mismatch between the left- and right-hand side terms in equation (1) can result in erroneous flaring angle and inaccurate prediction of the tail radius and magnetic flux. This can occur in case of (a) inhomogeneous solar wind or (b) incorrect propagation time delay estimates. In practice, we tackle these problems in two ways. First, given the relatively large solar wind travel times between the L1 point and the Earth, the timing accuracy of the OMNI 1 min average data (http://omniweb.gsfc.nasa.gov) is hardly trustworthy. For that reason, we base our method on 5 min-averaged data. Second, during sharp Pd jumps the pressure balance is violated, which makes the method inapplicable for those cases, and the corresponding time intervals should be flagged as questionable.

As can be seen from the above list, the MTF algorithm described by equations (1)–(5) includes a number of strong assumptions and caveats and, hence, may only provide a crude estimate of the tail flux and its variations. Before being accepted as a reliable tool, the method requires an extensive calibration and validation,

in order to identify its applicability domain and to provide proper correction factors. The calibration constitutes a delicate and important part of the method. Although no direct measurements of the magnetotail flux exist, fortunately enough, there are two natural ways to independently validate and calibrate the method. Both of them make it possible to calculate the MTF through a tail cross section at any particular state or time and simultaneously provide all the variables in equations (1) and (2), necessary to apply the algorithm and get the MTF estimate. One of these calibration tools is based on global 3-D MHD (GMHD) simulations, which solve the MHD equations and numerically simulate the magnetosphere based on first principles [see, e.g., *Raeder*, 2003]. Another possibility is provided by the recent empirical magnetospheric model T14 [*Tsyganenko*, 2014] which, unlike its predecessors, uses a magnetopause model with an IMF-dependent flaring rate (from *Lin et al.* [2010]) and is based on a significantly extended spacecraft database. Though another empirical model with IMF-dependent magnetopause was constructed more recently [*Tsyganenko and Andreeva*, 2015, TA15], we still chose the T14 version for this study, as TA15 is not designed to reproduce magnetospheric dynamics. These justification and calibration tools and their results are addressed in sections 3.1 and 3.2, respectively.

The algorithm results should also be compared with polar cap area observations based on global auroral images and measurements of the R1 field-aligned current oval position by the AMPERE experiment. These comparisons are presented in section 4 together with results of the algorithm application to THEMIS observations.

2.2. Extensions to Include the Inner Magnetotail Observations (F_1 and F_2 Algorithms)

The quantity of interest, the open magnetotail magnetic flux (MTF), is basically provided by the θ-shaped magnetotail currents with the corresponding magnetic field lines (B_{ext}) being schematically shown in Figure 2. However, in the inner magnetotail (earthward of 10–15 R_E) the dipole field provides a significant (if not dominant) contribution to the total B observed by the spacecraft. In this case the magnetic field forming the magnetotail flux, calculated in (5), is overestimated. Intuitively, Figure 2 suggests that a similar kind of algorithm may be tried out, in which the magnetic field of the tail current system alone (B_{ext}) is used, obtained by subtracting the dipole contribution (the IGRF field, *BD* in Figure 2) from the total observed magnetic field vector.

Following this conjecture, two MTF proxies were proposed in SG'15, denoted as F_1 and F_2 to distinguish them from F_0, the original solution of equations (1)–(5). These proxies are constructed as follows.

As in the original derivation, it is assumed that the "external" magnetic field is approximately uniform in the tail cross section. In the first case, as before, the flaring angle α is determined from (1) and is used to compute A^* and R_T from (4), but B_L in (5) is replaced by $B_{\text{ext}} = B - B_{\text{IGRF}}$ when finally calculating the magnetic flux:

$$F_1 = 0.5\pi R_T^2 B_{\text{ext}} \tag{7}$$

F_1 may be considered as an upper estimate of the open magnetic flux because (7) neglects the plasma sheet width, assuming the external field to be uniform in the entire cross section. This procedure indeed provides a reasonable MTF estimate based on observations in the inner magnetosphere, but on some occasions the algorithm fails: large B_L values in the inner magnetosphere sometimes lead to too large α values in (1), which require too large ΔX corrections, so that X^* may become positive; also, sometimes $\sin^2\alpha$ (determined from equation (1)) may become > 1.

To remedy these situations, another modification was tested, using only the external field in the right-hand side of (1), which gives

$$0.88Pd\sin^2\alpha_{\text{ext}} + B_{\text{sw}}^2/2\mu_0 + n_{\text{sw}}k_{T\text{sw}} = B_{\text{ext}}^2/2\mu_0. \tag{8}$$

Based on (8), we obtain a modified flaring angle α_{ext} and calculate the modified radius $R_{T\,\text{ext}}$ as

$$R_{T\,\text{ext}}(X^*) = R_{T0} - 2/C\left(\arcsin\left(A^*_{\text{ext}} \times \exp\left(CX^*/2\right)\right) - \arcsin\left(A^*_{\text{ext}}\right)\right). \tag{9}$$

As the dipole field is completely ignored in (8), the $R_{T\,\text{ext}}$ value provides rather a lower estimate of the magnetopause radius, and our new proxy F_2 can be treated as a lower MTF estimate:

$$F_2 = 0.5\pi R_{T\,\text{ext}}^2 B_{\text{ext}}. \tag{10}$$

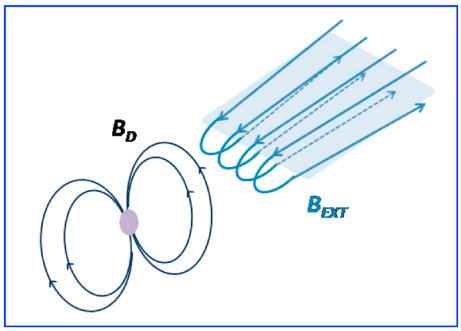

Figure 2. The schematic of the field lines of external (B_{EXT}) and internal (IGRF, B_D) magnetic fields in the magnetotail.

In this case, when projecting the spacecraft location to the magnetopause we assume that the contours of $B_{\text{ext}} = \text{const}$ are perpendicular to the magnetopause. This assumption will be illustrated and verified below along with the assumption of B_{ext} uniformity.

A special comment should be made concerning a difficulty when attempting to use the observations from the near-equatorial (plasma sheet) region in the inner magnetosphere. While the variable $\mathbf{B_{ext}} = \mathbf{B} - \mathbf{B_{IGRF}}$ has an obvious interpretation in the tail lobes, it is much less clear how to define the equivalent external lobe field in the plasma sheet. In SG'15 we formally defined it through the equation

$$B^2_{L\,\text{ext}}/2\mu_0 = B^2_{\text{ext}}/2\mu_0 + nkT. \tag{11}$$

However, while in the tail lobes the angle between the vectors $\mathbf{B_{ext}}$ and $\mathbf{B_{IGRF}}$ does not usually exceed ~90°, in the plasma sheet they may become antiparallel (see Figure 2). In particular, $|\mathbf{B_{ext}}|$ may exceed measured $|\mathbf{B}|$ and, according to (11), the "equivalent external pressure" will exceed the total pressure, which is senseless. So $B_{L\,\text{ext}}$ is correctly defined only in the tail lobes. In view of that, we confine our calculations of F_1 and F_2 to only the tail lobes, defined hereafter as the region with plasma $\beta < 1$. As in SG'15, to further filter out questionable data inside the plasma sheet, we calculated $B_{L\,\text{ext}}$ from (11) only if the angle between $\mathbf{B_{ext}}$ and $\mathbf{B_{IGRF}}$ was less than 90°.

3. Calibration of the Method

3.1. Calibration Tools for MTF Calculations

As pointed out in section 2, the MTF calculations by means of equations (1)–(5) and their above described extensions are based on approximate relationships, whose derivation included strong assumptions and caveats. An independent testing and validation of the proposed MTF proxies should provide proper correction factors and establish their applicability domains. Two independent ways were followed in this work to validate and calibrate our algorithms, each providing all variables required to evaluate F_0, F_1, and F_2 quantities and, at the same time, making it possible to calculate the reference MTF through any tail cross section and compare it with these estimates.

The first way was to use the results of global 3-D MHD simulations of the magnetosphere [e.g., *Raeder*, 2003, which is quite a natural choice, since the MTF algorithm is based on MHD pressure balance equations. Four GMHD codes are available at NASA Community Coordinated Modeling Center (CCMC, http://ccmc.gsfc.nasa.gov): BATS-R-US [*Powell et al.*, 1999] hereafter denoted as BRS (reference flux FBRS); Open GGCM [*Raeder et al.*, 2008], hereafter OGM; LFM [*Lyon et al.*, 2004]; and GUMICS [*Janhunen et al.*, 2012]. All the codes solve numerically the ideal MHD equations, however, using different numerical solvers and different grids.

In a recent extensive validation study by *Gordeev et al.* [2015] it was found that CCMC-operated GMHD models can correctly reproduce some elements of the large-scale magnetospheric configuration (size and shape of magnetosphere, convection patterns, FACs), both in static and dynamic regimes during the loading-unloading cycle. However, the models differently reproduce the magnetospheric parameters and their behavior. Overall, the best validation scores for the key system parameters, describing global equilibrium, were shown by BATS-R-US, whereas LFM and Open GGCM codes were found to better reproduce the dynamical loading-unloading (substorm) cycle characteristics [*Gordeev et al.*, 2015]. Bearing it in mind, we tried to avoid model-dependent features when using results of the three models for testing the method of MTF calculation. The GUMICS code failed to satisfactorily describe the substorm dynamics and thus was excluded from the following analysis.

As an input for CCMC simulations we used synthetic solar wind conditions with an IMF B_z component (Figure 3) varying between northward and southward directions with 1–2 h period to reproduce substorm loading-unloading sequence, with other SW/IMF parameters (IMF B_x = IMF B_y = 0, $V_x = -300$ km/s, $V_y = V_z = 0$, $N = 20$ cm^{-3}) being kept unchanged. The proton temperature was held $1.6 \cdot 10^5$ K during the

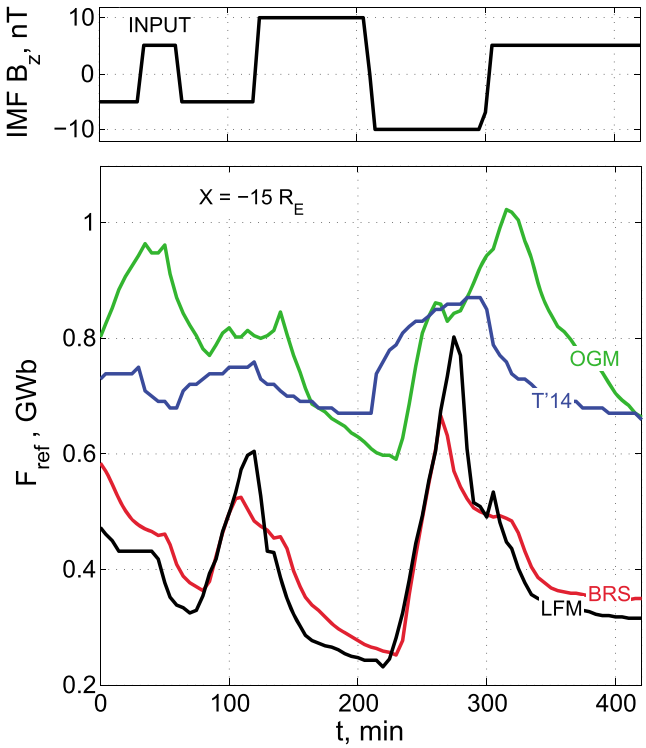

Figure 3. Reference MTF values in GMHD simulations (OGM for Open GGCM and BRS for BATS-R-US) and in T14 for the idealized solar wind input shown in the upper panel.

periods 0–120 min, 300–420 min, while being lowered down to $5.2 \cdot 10^4$ K the rest time. We also set the dipole tilt at zero and used a constant ionospheric conductance model with equal Hall and Pedersen conductivities $\Sigma H = \Sigma P = 5$ Mho. All the data for F_1 and F_2 computations were taken from the corresponding simulation.

To calculate a reference MTF value to be compared with our algorithm estimates, we performed a direct numerical integration of the magnetic flux through a chosen tail cross-section $X = -15\ R_E$. At that distance, the tail approximation is already satisfied, whereas the grid resolution of the GMHD models is still reasonably good. In all the models the grid spacing rapidly grows down the tail, which degrades the accuracy of the magnetopause determination and the magnetic field integration. The outer integration boundary was the magnetopause, identified here as the fluopause, i.e., the surface formed at each time step by the innermost plasma flow lines traced from the solar wind down the magnetotail [*Palmroth et al.*, 2003]. Separation between the magnetic flux in the northern and southern lobes was based on the sunward/tailward magnetic field direction. More details on the magnetic flux calculation in GMHD simulations can be found in *Shukhtina et al.* [2009].

The second independent calibration tool is provided by the recent empirical T14 magnetospheric model [*Tsyganenko*, 2014], based on an extended spacecraft data base. The model uses an advanced empirical magnetopause based on *Lin et al.* [2010] model with IMF-dependent flaring rate. The T14 model is driven by a set of parameters quantifying the competition between the external driving by the solar wind and internal losses and, as such, replicates the large-scale reconfiguration of the magnetosphere during storms. However, it cannot by construction reproduce the substorm dynamics. Also, the model does not describe the magnetospheric plasma distribution; for that reason we somewhat conventionally defined the tail lobes as the regions with $|Z| > 5\ R_E$.

The simulated F_{ref} behavior for three GMHD models and T14 is shown in Figure 3. We see that in different models F_{ref} variations strongly differ from each other, both in amplitude and in shape. The F_{ref} values given by BATS-R-US and LFM are substantially smaller(sometimes more than twice) than those in Open GGCM; the F_{ref} values in T14 are somewhere between those in the GMHD models. The dynamics is also quite variable: in the GMHD simulations we observe sudden substorm-like unloadings occurring at different times in different models. By contrast, there are no substorms in the T14 model, and the F_{ref} variations take place only

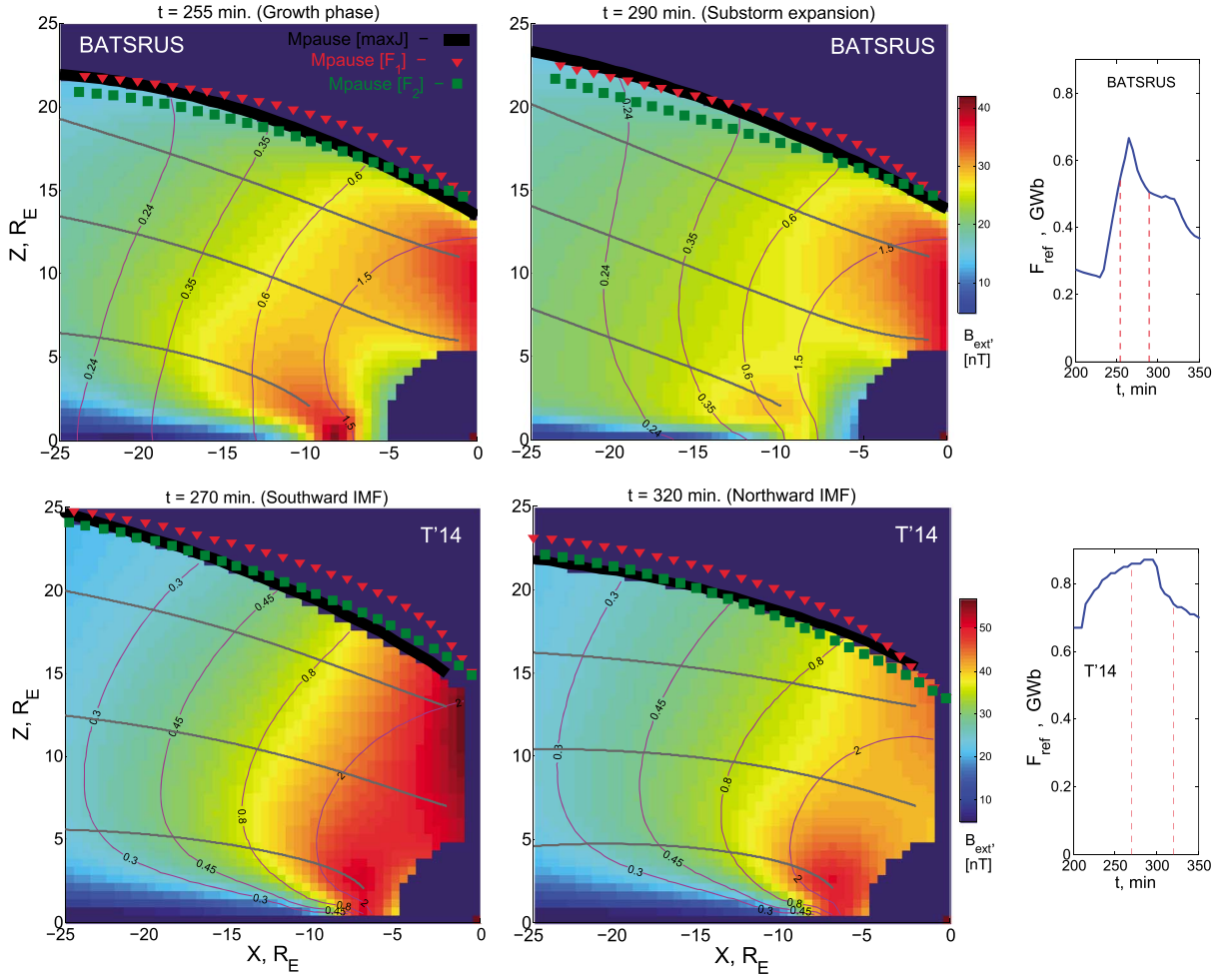

Figure 4. Results of the simulations (top row) BATS-R-US_Gordeev_110309_1 and (bottom) T14 in the meridional magnetosphere section $y = 0$ before and after unloading. F_{ref} variations are shown on the right, vertical dashed lines indicating the times of corresponding snapshots. Black lines are the B_{ext} field lines, B_{ext} values being shown by color. Total pressure (in nPa) isolines are shown in magenta. The solid black line indicates the model magnetopause, whereas the red triangles and green squares designate the R_T and $R_{T\,ext}$ position.

as an ordered response to the external driving. As the pressure balance is automatically fulfilled in GMHD simulations, we believe that our MTF derivation algorithm is appropriate for any GMHD model, regardless of its numerical specifics. Unlike in the first-principle simulations, the empirical T14 is not force-balanced by construction, which makes it all the more interesting to test that model in our algorithm.

Besides comparing the MTF values, our calibration approach allows one to monitor other important parameters of the system. Figure 4 (top row) shows snapshots of the midnight tail section for BATS-R-US simulation before and after unloading (vertical dash lines in the right panel). The color-coded B_{ext} magnitude distributions reveal that B_{ext} is approximately uniform in the tail sections. One can also see that B_L isointensity lines (magenta) are roughly normal to the magnetopause in the tail lobe region at $X<-5\ R_E$ (excluding the region adjacent to magnetopause tailward $-20\ R_E$); the same is approximately fulfilled for B_{ext} isointensity lines (perpendicular to black B_{ext} field lines). Three magnetopause proxies, including the fluopause (thick black line) and those based on the tail radius estimates R_T and $R_{T\,ext}$ from equations (4) and (9), are also shown. Red triangles and green squares denote the boundary locus points, obtained by placing a virtual spacecraft at a set of equidistant locations $[X_i, 0, 14\ R_E]$ with X_i running between 0 and $-25\ R_E$ at 1 R_E step, and calculating the tail radii from equation (4) (red) and equation (9) (green), respectively. As clearly seen from the plots, the fluopause is straddled between the bound aries, obtained by calculating R_T and $R_{T\,ext}$.

Figure 4 (bottom row) shows the result, obtained by the same method but using the empirical model T14; in this case the *Lin et al.* [2010] magnetopause is plotted instead of the fluopause. Unlike in the MHD simulation,

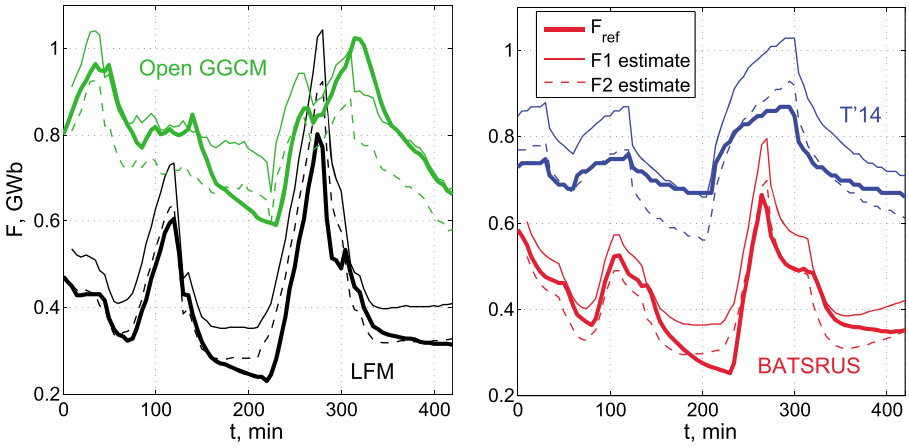

Figure 5. F_1 and F_2 variations based on observations at (−15, 0, 10) compared with variations of the reference magnetic flux F_{ref} for three GMHD simulations and T'14.

the general magnetopause shape is close to the surface, corresponding to $R_{T\,ext}$ (equation (9)). The requirements that B_{ext} be uniform and B_L (to a lesser degree for for B_{ext}) isointensity lines be normal to the magnetopause are approximately met.

Summarizing, we conclude that (1) the fluopause in the BATS-R-US model on the average lies between R_T and $R_{T\,ext}$ proxies whereas the Lin's magnetopause shape is adequately reproduced by the $R_{T\,ext}$ estimate; (2) our major assumptions: nearly uniform B_{ext} in the lobes and nearly perpendicular orientation of B_L = const and of $B_{L\,ext}$ = const lines to magnetopause (used in spacecraft projecting to the magnetopause), are reasonable (although not perfect) approximations.

3.2. Calibration and Justification of the MTF Calculations

Having ensured that our basic assumptions are approximately satisfied, we proceed to the analysis of results. In SG'15 it was shown that even at $X = -15\ R_E$ (and even more so at closer geocentric distances) the F_0 algorithm gives overestimated the MTF due to the dipole contribution. As we are going to test the method in the entire inner and middle (at $X = (-5,-25\ R_E)$) tail, we temporarily exclude the F_0 algorithm from consideration, confining ourselves to F_1 and F_2. We investigate if the formulas (7) and (10) may provide a good quantitative agreement between the MTF prediction and reference tail magnetic flux F_{ref} and determine the application domains of the F_1 and F_2 proxies.

3.2.1. Comparison of Different Models and Illustration of the Testing Procedure

To test our F_1 and F_2 algorithms, we applied them to three MHD simulations and the T14 model, with the same input as shown in Figure 3 (top). All the parameters required by a given algorithm were taken directly from the corresponding simulation. The testing procedure compared the algorithm proxies with the reference magnetic flux values, obtained by direct integration over the tail cross-section $X = -15\ R_E$.

Figure 5 compares the MTF model estimates with their reference values. Here F_1 and F_2 values were computed based on the lobe magnetic field observed at a single point in the lobes at [−15, 0, 10] R_E. As was pointed out earlier, the reference flux values differ significantly for different models (Figure 3). However, according to Figure 5, in each case the F_1 and F_2 vary in a consistent manner and have similar absolute values as those of the corresponding reference flux. This kind of agreement has been noticed in previous comparisons [*Shukhtina et al.*, 2009; SG'15] and opens a possibility for the code-independent calibration of the method. For Open GGCM and BATS-R-US the reference flux F_{ref} stays in between F_1 and F_2 values (as expected, see section 2.2), whereas for LFM and T14 it is closer to the F_2 estimate. During the long period of strong northward IMF (between t = 160 and 220 min) the behavior changes: in MHD both F_1 and F_2 exceed F_{ref}, whereas for T14 F_{ref} approaches the F_1 value (being close to F_2 during other periods).

It should also be noticed that the amplitude of variations of F_1 and F_2 estimates exceeds that of F_{ref} for T14 (which mainly results from different flux variations at northward IMF), whereas in MHD models those amplitudes are approximately the same.

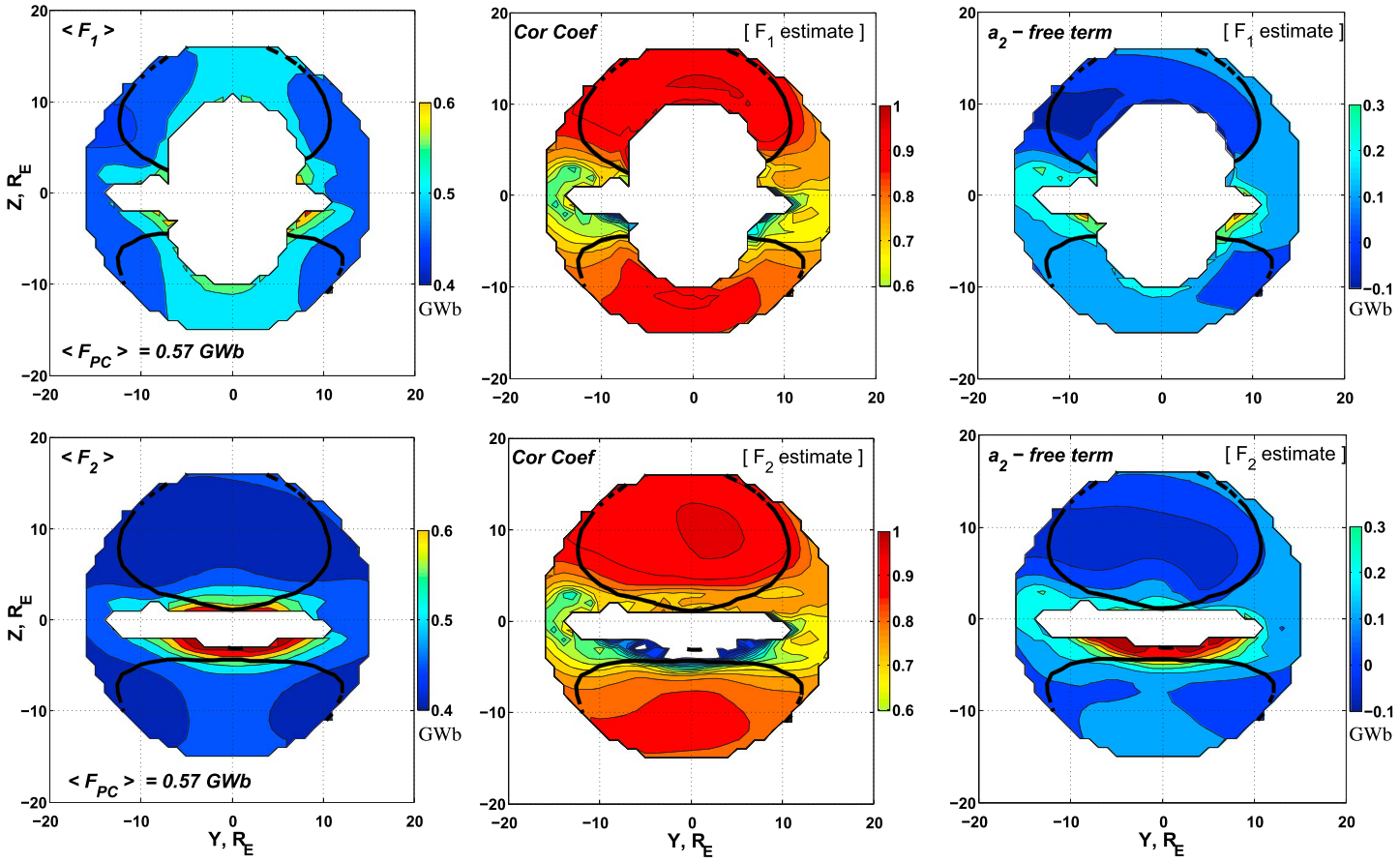

Figure 6. Distributions of the average over the simulation flux value, correlation coefficient with the reference flux, and the free term for F_1 and F_2 algorithms (simulation BATS-R-US_Sergeev_060508_1) across the cross-section $X = -7\ R_E$. Black thick contour on each panel bounds the lobes with $\beta < 1$.

3.2.2. MHD/T14—Global Tests, Calibration, and Errors

Figure 5 displays the results of testing the method at only a single location. To evaluate the overall quality of the method, it is necessary to fulfill a statistical analysis in the entire region where MHD simulations are reliable (earthward of $X = -25\ R_E$, see above) and identify the region (applicability domain) where the method gives satisfactory results. Good quality means high and stable correlation coefficients, with the regression coefficients close to unity.

Before presenting the results, some comments are in order. First, in *Shukhtina et al.* [2009, 2010] it was found that, during the substorm expansion phase, the F_0 algorithm degrades at locations inside the plasma sheet (i.e., with high plasma β) due to the breakdown of the 1-D pressure balance. It should also be remembered that the F_1 and F_2 proxies are not applicable in the plasma sheet, whereas the F_0 modification can be used only in the regions, where the tail approximation is roughly fulfilled. Next, the analysis in SG'15 revealed that the quantities F_1 and especially F_2 are uniform across the tail for various Y and Z locations at a given constant X, and the free term in the regression equation $F = a_1 F_{\text{ref}} + a_2$ is small. Figure 6 shows spatial distribution of statistical parameters of both F_1 and F_2 calculated for a real event simulation BATS-R-US_Sergeev_060508_1 from SG'15. The figure displays distributions of the average over the simulation interval MTF value (left), of its correlation coefficient with F_{ref} (center), and of the free term (right), in the cross section $X = -7\ R_E$. Here the F_{ref} was defined as the magnetic flux FPC through the polar cap, obtained from the MHD simulation. Figure 6 demonstrates a uniform distribution of all considered parameters, high (> 0.8) *CC* value and small (< 0.1 GWb) free term. The small free term justifies its omission in the regression equation, which therefore takes the simplest form: $F_{1,2} = K F_{\text{ref}}$ with the proportionality factor K. A remarkable feature apparent in Figure 6 is that the F_2 quantity may be calculated (with a result almost independent of the observation point) in the entire tail lobe volume, in contrast to F_1, confined to the narrow high-latitude ring. Note that according to SG'15,

Table 1. Statistical Characteristics (Proportionality Factor *K*, Correlation Coefficient *CC*, Standard Deviation SD (GWb), and the Number of Data Points *N*) at Different Tail Cross Sections, Obtained for Different Models

	$X = -5\ R_E$	$X = -7\ R_E$	$X = -11\ R_E$	$X = -15\ R_E$	$X = -25\ R_E$
	K (*CC*) SD N	K (*CC*) SD N	K (*CC*) SD N	K (*CC*) SD N	K (*CC*) SD N
			LFM		
F_1	1.32 **(0.82)** 0.07 8591	1.34 **(0.85)** 0.07 16366	1.30 **(0.91)** 0.07 26854	1.30 **(0.94)** 0.06 30385	1.31 **(0.88)** 0.12 32518
F_2	1.19 (0.63) 0.09 16497	1.16 (0.79) 0.08 22122	1.15 **(0.91)** 0.07 28818	1.17 **(0.92)** 0.07 31921	1.24 **(0.87)** 0.12 34788
			BRS		
F_1	1.13 (0.74) 0.05 8686	1.14 (0.71) 0.06 17694	1.15 **(0.82)** 0.06 24982	1.18 **(0.90)** 0.05 23771	1.25 **(0.87)** 0.07 15715
F_2	1.02 (0.41) 0.09 15753	1.00 (0.57) 0.08 21868	1.01 (0.79) 0.07 24982	1.06 **(0.85)** 0.06 23771	1.18 **(0.85)** 0.07 15715
			OGM		
F_1	0.88 (0.71) 0.07 6179	0.94 (0.71) 0.07 12854	1.01 (0.66) 0.08 23797	1.03 (0.63) 0.08 24842	1.08(0.28) 0.10 24201
F_2	0.78 (0.65) 0.08 14885	0.82 (0.62) 0.09 19169	0.90 (0.63) 0.08 24509	0.94 (0.61) 0.08 24842	1.03 (0.33) 0.10 24201
			T14		
F_1	0.95 **(0.84)** 0.06 11511	1.00 **(0.87)** 0.05 22187	1.04 **(0.85)** 0.06 50858	1.02(0.79) 0.07 72014	0.88(0.51) 0.10 100846
F_2	0.81(0.79) 0.07 21664	0.87 **(0.85)** 0.05 31875	0.92 **(0.87)** 0.05 51620	0.92 **(0.87)** 0.06 72014	0.82 (0.55) 0.09 100659

[a]High-correlation coefficients ($CC > 0.8$) are highlighted in bold.

FPC well correlates ($CC = 0.85$) with the directly integrated MTF value (excluding time intervals with a strong positive IMF B_z).

Now the critical question is how the MTF prediction (i.e., the *K* coefficient and the correlation coefficient *CC*) changes with distance downtail, in the regions with different relative contributions of the external and dipole field to the total *B*. To answer this question, we analyzed separately all the points in the tail cross sections at $X = -5, -7, -11, -15, -25\ R_E$ for $|Y| < |X|, \beta < 1$ (tail lobes) at $1\ R_E$ step in *Y* and *Z*. In the case of T14 model, the region with $|Z| < 5\ R_E$ was conventionally excluded from the tail lobes. Table 1 presents the information about the proportionality coefficient *K*, the correlation coefficient *CC*, the standard deviation of predictions, and the total number of analyzed points in each cross-section. The table reveals the following important results:

1. The proportionality factor *K* is stable (to within 10%) at different distances, for each quantity (F_1 or F_2), and for each model. This implies a possibility to construct a global regression equation for each quantity and each model for the calibration purposes.
2. In most cases the comparison shows a good correlation between the MTF algorithm predictions and F_{ref}. The correlation is especially high ($CC > \sim 0.8$ in 9 of 10 predictions) and uniformly good at different *X* for the LFM model, while the worst correlations were found for the Open GGCM model, whose quality progressively degrades downtail. An encouraging feature is that a generally good prediction was found in the innermost distance range ($X = -5R_E$), justifying our efforts (section 2.2) to extend the MTF derivations to the inner dipole-dominated region.
3. The *K* values slightly differ between different models, varying in the range 0.8 to 1.3; hence, $K = 1$ can be viewed as a reasonable average value.

Note the difference in the number of data points *N* used to evaluate F_1 and F_2 earthward $-15\ R_E$. The smaller numbers for F_1 as compared to F_2 are due to the absence of solutions for F_1 in some cases, most of which correspond to the innermost distances, as discussed above in section 2.2.

Results concerning the T14 model deserve a separate discussion. It is the only model where the free term in the regression equation is not small, and the regression coefficient a1 strongly differs from 1. For the *X* interval $(-5, -15\ R_E)$ we found $< a_1 > = 1.6, 1.5$; $< a_2 > = -0.4$ GWb, -0.5 GWb for F_1 and F_2, respectively. As already mentioned, the large difference between the amplitudes of *F* variation is mainly observed during the interval of large positive IMF B_z (Figure 5). Though the *K* coefficient is close to unity and despite the high correlation coefficient, given by the simplified equation $F_1, 2 = k\ F_{ref}$, the algorithm on average exaggerates the amplitudes of flux variations by the factor ~ 1.5. This effect grows earthward and peaks at $X = -5\ R_E$ with $a1 = 1.9$ and 1.6 for F_1 and F_2, respectively. At $X = -25\ R_E$ the situation is opposite: $a_1 \sim 0.8, a_2 \sim -0.1$ for both F_1 and F_2, but correlation is low ($CC \sim 0.5$). The whole regression equations at different distances are presented in Table S1.

Table 2. Average Prediction Relationships for T14 and MHD Models

	T'14	BATS-R-US	LFM	Open GGCM
F_1	$F_1 = 1.02 * F_{T14}$	$F_1 = 1.17 * F_{BRS}$	$F_1 = 1.30 * F_{LFM}$	$F_1 = 1.00 * F_{OGM}$
	$CC = 0.81$	$CC = 0.82$	$CC = 0.85$	$CC = 0.60$
	SD = 8%	SD = 12%	SD = 15%	SD = 11%
F_2	$F_2 = 0.90 * F_{T14}$	$F_2 = 1.07 * F_{BRS}$	$F_2 = 1.21 * F_{LFM}$	$F_2 = 0.89 * F_{OGM}$
	$CC = 0.81$	$CC = 0.72$	CC = 0.81	$CC = 0.53$
	SD = 9%	SD = 17%	SD = 18%	SD = 15%

Having thus established the stability of the proportionality coefficient K and CC values along and across the tail for the models under consideration, we turn to constructing average prediction relationships for the near/middle tail for each model. The results are presented in Table 2. For BATS-R-US and LFM the whole tail lobe volume between $X = -5$ and $-25\ R_E$ was considered, whereas for T14 and Open GGCM the tailward boundary was set at $X = -15\ R_E$. As pointed above according to Tables 1 and 2 the value $K = 1$ may be taken as the reasonable common calibration factor.

3.2.3. Application Conditions and Validity Domains to Compute F_0, F_1, and F_2 MTF Proxies

Now we summarize the available information about application conditions and domains of the method (Table S2 in the supporting information).

1. The initial F_0 algorithm [*Shukhtina et al.*, 2009] presumes that the tail approximation is valid. It is usually considered to be the case tailward from $-15\ R_E$, though it may occasionally be violated in that region (e.g., in plasmoids and BBFs) and, on the other hand, be true earthward from $-15\ R_E$ when the field is strongly stretched. The F_0 algorithm was based on Geotail data set, which contained tail data with $X<-15\ R_E$, $|Y|<15\ R_E$ corresponding to the presumed F_0 application domain.
2. Our tests (Tables 1 and 2) were performed for F_1 and F_2 at $X(-5\ R_E, -25\ R_E)$, $|Y| < |X|$. According to Table 1, all models (excluding BATS-R-US for F_2 at $X = -5\ R_E$) manifest satisfactory results (with $CC \geq 0.6$) for $X(-5\ R_E, -15\ R_E)$; for BATS-R-US and LFM the tailward boundary is at $-25\ R_E$. The condition $|Y| < |X|$ is preserved in all cases.
3. MHD tests in *Shukhtina et al.* [2009] showed that the F_0 variations are better reproduced based on measurements in the tail lobes, rather than in the plasma sheet. In that study, the virtual spacecraft were placed in the tail regions with different plasma β values, and the obtained F_0 variation was compared with F_{ref} for the given simulation. It was found that the CC values decreased with growing plasma β; according to the MHD tests, such failures were due to the pressure imbalance in the plasma sheet during the expansion phase.
4. It was also found [*Shukhtina et al.*, 2010] that the F_0 estimates substantially exceeded those based on optical PC observations during long periods of positive IMF B_z. As discussed above, the relation between F_1/F_2 proxies and F_{ref} also change during such intervals (differently for different models, Figure 5). Therefore, such periods should be also flagged (i.e., analyzed separately).
5. The pressure balance also breaks down during *Pd* jumps, which makes such events problematic for the method. Besides, such jumps may be a source of additional confusion in the results, due to wrong timing.
6. One more factor is the dipole tilt angle Ψ. Whereas in the middle tail (tailward of 10–15 R_E) the assumed geometry (presented in Figure 1) is more or less preserved for tilted dipole (with the shifted neutral sheet), earthward of 10 R_E it is strongly violated.

4. Observation-Based Validation

As a part of European Cluster Assimilation Technology (ECLAT) project, a data set of F_1 and F_2 estimates for 2001–2009 has been created. It is based on solar wind observations and Cluster magnetic field measurements, in which an advantage was taken of the inclined Cluster orbit traversing the tail lobes. These data are available through the Cluster Science Archive http://www.cosmos.esa.int/web/csa. Here we used Cluster data at 5 min resolution, obtained by averaging the original 4 s Cluster magnetic observations from CDAWeb; solar wind observations were presented by 5 min OMNI data, propagated from upstream monitors to the bow shock and then time shifted to the Cluster X position with the solar wind speed. Identification of different tail regions tailward of $X = -8\ R_E$ for the Cluster tail seasons 2001–2009 has also been done under the ECLAT project and is available through the Cluster Science Archive; based on that identification, we selected observations

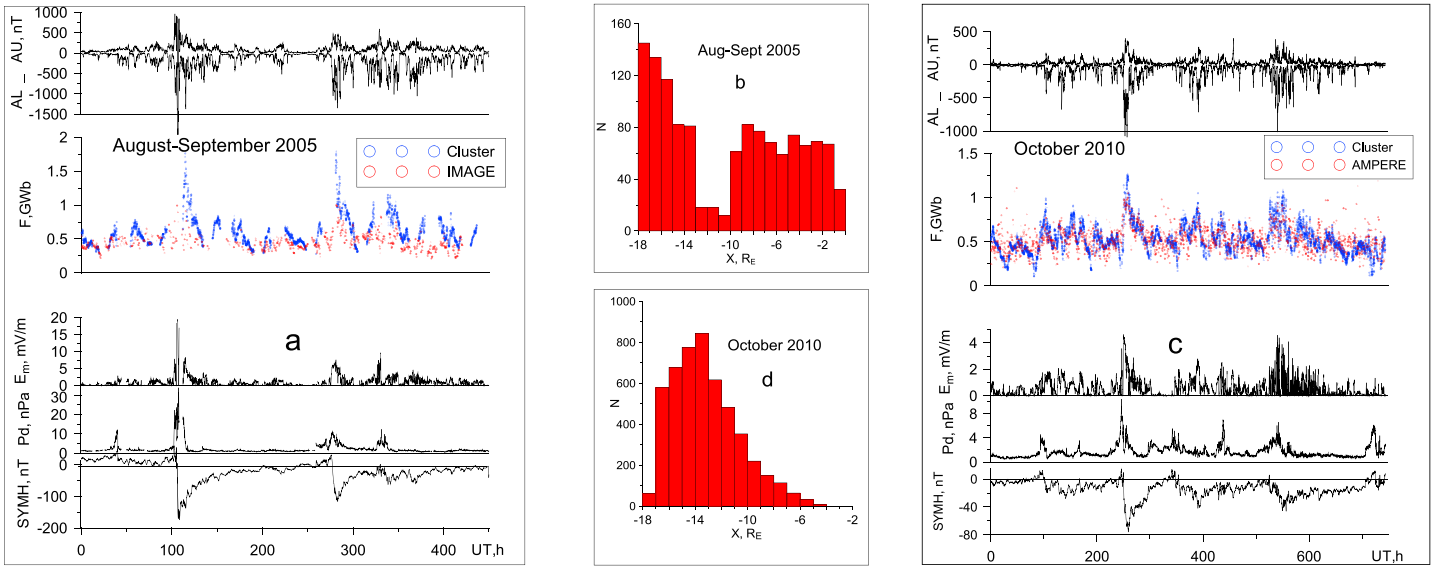

Figure 7. Comparison of F_2 values, based on Cluster measurements, with F_{PC} estimates, based on (a) IMAGE global auroral images and (c) AMPERE polar cap observations. (b and d) Cluster *X* coordinate distribution.

in the tail lobes and plasma sheet boundary layer for our F_1, F_2 calculations. For Cluster observations earthward $-8\ R_E$ and for the period October 2010 we identified the tail lobes by visually inspecting the Cluster quicklook plots (http://www.cluster.rl.ac.uk/csdsweb-cgi/csdsweb_pick). The MTF data are also available on http://geo.phys.spbu.ru/eclat/.

4.1. Comparison With Global Auroral Images (IMAGE Data)

We studied the period 20 August–6 September 2005 characterized by variable geomagnetic activity, including quiet periods, several dozens of substorms and two storms. Data on the open magnetic flux were presented in *Milan et al.* [2008]. The images were obtained by Wideband Imaging Camera of the far ultraviolet Imager (FUV/WIC) on board the IMAGE spacecraft.

A survey of the time interval studied is displayed in Figure 7a. Along with the magnetic flux estimates, the plots present interplanetary parameters and geomagnetic indices *AU*, *AL*, and *SYM-H*. The external parameters are the solar wind dynamic pressure *Pd* and the "merging electric field" $E_m = V B_T \sin^3 \theta/2$ [*Boyle et al.*, 1997]. The Cluster data are represented by the F_2 values based on Cluster 4 observations. The F_2 data set is chosen because it is much larger than the F_1 set (1146 points against 741), which is due to the fact that owing to the orientation of the Cluster orbit (Figure 7b), about half of observation points lie inside $X = -10\ R_E$, many of them close to terminator. The results of regression analysis are displayed in Table 3, from which (as well as from a direct visual inspection) one sees that both F_1 and F_2 values are larger than those obtained from the optical observations. The average proportionality coefficients for F_1 and F_2 (equal to the ratio of the average

Table 3. Results of the Regression Analysis of F_1 and F_2 Quantities, Using Cluster Tail Data, With FPC Values Based On IMAGE Images and AMPERE Magnetic Measurements

	IMAGE	AMPERE
F_1	$F_1 = 1.25\,F_{IM} + 0.15$	$F_1 = 0.87\,F_{AMP} + 0.20$ GWb
	$CC = 0.72$, $N = 741$, SD = 0.16 GWb(36%)	$CC = 0.72$, $N = 2049$, SD = 0.12 GWb (23%)
	$< F_{IM} > = 0.44$ GWb, $< F_1 > = 0.71$ GWb	$< F_{AMP} > = 0.53$ GWb, $< F_1 > = 0.66$ GWb
	$< F_1 > / < F_{IM} > = 1.6$	$< F_1 > / < F_{AMP} > = 1.2$
F_2	$F_2 = 1.26\,F_{IM} + 0.05$ GWb	$F_2 = 0.82\,F_{AMP} + 0.16$ GWb
	$CC = 0.69$, $N = 1146$, SD = 0.16 GWb (36%)	$CC = 0.70$, $N = 2238$, SD = 0.11 GWb (21%)
	$< F_{IM} > = 0.45$ GWb, $< F_2 > = 0.63$	$< F_{AMP} > = 0.53$ GWb, $< F_2 > = 0.59$ GWb
	GWb $< F_2 > / < F_{IM} > = 1.4$	$< F_2 > / < F_{AMP} > = 1.1$

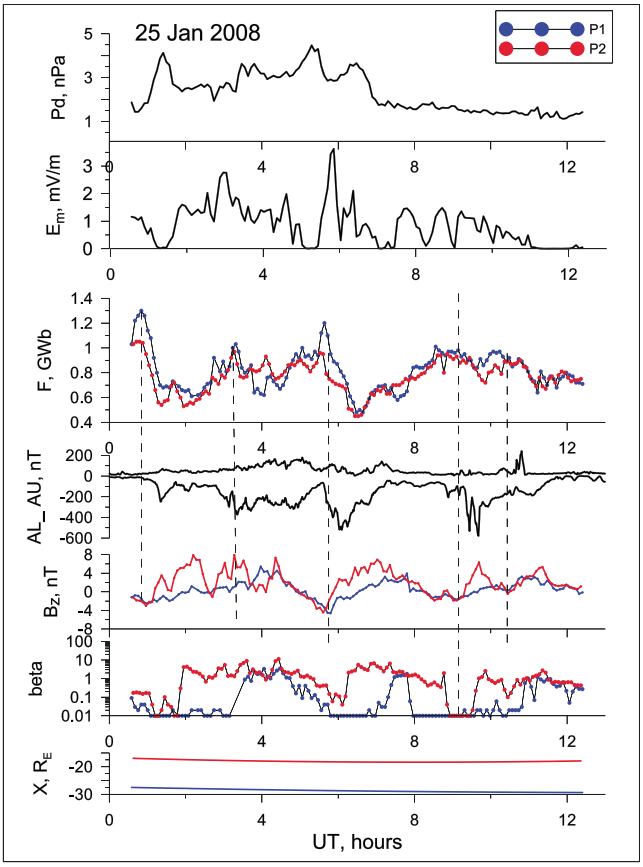

Figure 8. An example of F_{P1} and F_{P2} variations, together with other parameters' behavior.

flux values, see Table 3) are 1.6 and 1.4, respectively. The free term is rather small, especially for F_2. The largest inconsistencies are observed in the case of the storms associated with large negative *SYM-H* index and large *Pd* pulses, not suitable for our method.

4.2. Comparison With AMPERE Data

The method of the open magnetic flux calculation using AMPERE data is described in *Clausen et al.* [2012]. It is based on the identification of R1 currents' oval, which was shown to statistically collocate with the polar cap boundary [*Clausen et al.*, 2013]. For comparison, we chose the period of October 2010, when Cluster was mostly in the lobes. The selected period was mainly characterized by high activity, favorable for the AMPERE method, and included two storms — see *SYM-H* and *AL* variations in Figure 7c. The figure also presents F_2 values based on Cluster measurements, along with the AMPERE open flux estimates. For the AMPERE magnetic flux values we took the average of 2 min values in the Northern and Southern Hemispheres. For the regression analysis, these values were recalculated into 5 min averages. The results of analysis are also presented in Table 3. Different from comparison with IMAGE data, the proportionality coefficients for F_1 and F_2 proxies are close to unity (1.2 and 1.1, respectively), whereas the correlations are the same (∼0.7) with a moderate free term.

4.3. Cross Validation Based On THEMIS Observations in the Plasma Sheet

Two THEMIS spacecraft in low-inclination orbits (probes P_1 and P_2) had their apogees in the midtail during the tail season January–April 2008, allowing us to compare the simultaneous MTF values estimated separately at different distances. The observations were made at ($X \sim -15 - -30\ R_E$), where the tail approximation is valid and the F_0 proxies were computed.

An example in Figure 8 presents THEMIS-based F_{P1} and F_{P2} variations together with the solar wind parameters and ground auroral indices during high geomagnetic activity. Despite a large separation between the P_1 and P_2 spacecraft, located at $X \sim -30$ and $-20\ R_E$, respectively, the calculated flux variations are similar and

Table 4. Comparison of MTF Values Derived From Spatially Separated THEMIS Spacecraft Data $F_{P2} = a_1 F_{P1} + a_2$.

	a_1	a_2, GWb	CC	SD, GWb	N	$< F_{P1} >$, GWb	$< F_{P2} >$, GWb	$< \Delta X >$, R_E	$< \Delta r >$, R_E
$X < -15\ R_E$	0.96	0.04	0.86	0.08	2000	0.72	0.74	7.8	8.2
$X < -15\ R_E$, $\beta < 0.37$	1.01	0.03	0.90	0.07	586	0.79	0.75	8.8	9.1
$X < -12\ R_E$	0.90	0.08	0.85	0.08	2835	0.73	0.72	6.4	6.7

show the correspondence with *AL* variations: each flux decrease being associated with *AL* decrease and the tail field dipolarization.

Table 4 provides a summary of THEMIS magnetic flux (F_0) comparisons made during the 2008 tail season. It reveals a consistency between the MTF values obtained by spacecraft separated (in average) by 6 to 10 R_E along the tail: the average flux values $<F>$ are similar, as well as their variations ($CC \sim 0.9$, regression slope $a_1 \sim 1$, with a small free term a_2). By extending the earthward boundary of observation region from 15 R_E to 12 R_E (last line), the results slightly degrade but still are acceptable. By using only the data in the lobes (corresponding to plasma $\beta > 0.37$), we observe a slight improvement of the regression and correlation (even although the spacecraft separation increases). Anyway, these comparisons confirm a low sensitivity of the MTF proxy to the actual distance of the observing tail spacecraft, which is an important step in the method validation.

5. Concluding Remarks

The method of in situ MTF calculation (equations (1)–(5)), based on the *Petrinec and Russell* [1996] ideas, was generalized and extended into the inner magnetosphere domain down to $-5\ R_E$ (equations (7)–(10)) with an improved formula for the magnetopause radius at terminator (equation (6)). Testing of the method based on three GMHD models and empirical T14 model demonstrated consistency of the results along and across the tail and allowed us to obtain the calibration coefficients (Tables 1 and 2). Although the differences of calibration coefficients in different GMHD models leave us some room for future improvement, these coefficients are all close to 1, justifying the usage of the algorithm in the existing form. The application domains of the algorithms have also been established (Table S2). Cross validation of the method based on two spatially separated (by 6–10 R_E in X) THEMIS spacecraft confirmed a low sensitivity of the MTF proxy to the actual distance of the observing tail spacecraft.

Comparison of the MTF estimates based on Cluster tail lobe observations with the estimates of the polar cap magnetic flux based on global auroral images and global FAC distributions (AMPERE project) provided some support (correlation coefficient $CC \sim 0.7$) but revealed also the quantitative differences in optical image-based and global FAC-based MTF estimates. In particular, our MTF values were found to be by a factor ~1.5 larger than the open flux values obtained by IMAGE, but similar to those derived from AMPERE. Each method has its own deficiencies, and at the moment it is unclear, which one is superior to others.

As the magnetotail magnetic flux is one of the global key parameters of the magnetosphere , its knowledge helps us to address fundamental problems of the magnetospheric dynamics. Some examples of recent applications are as follows:

1. It was statistically demonstrated that the amount of MTF increase in the magnetotail during the substorm growth phase approximately equals the magnetic flux threading the auroral bulge during the subsequent substorm expansion phase [*Shukhtina et al.*, 2005]. In this way, for the first time, the loading-unloading paradigm based on the idea of Dungey cycle, has been proved quantitatively in the global scale.
2. The hypothesis that the MTF must reach some critical value to initiate the substorm onset [e.g., *Freeman and Farrugia*, 1999] has been refuted. It was shown that the MTF value at the substorm onset is proportional to the merging electric field E_m, averaged over an hourlong period preceding the onset, and hence, no such thing as the critical flux value does exist [*Shukhtina et al.*, 2005]. The absence of the critical flux level was further confirmed in *Milan et al.* [2007], *DeJong et al.* [2007], *Boakes et al.* [2009], and *Shukhtina et al.* [2010].
3. Using the tail flux variations obtained by means of the present method, a new "balanced tail flux" type of substorms has been distinguished [*Shukhtina et al.*, 2014]. Such events, in which the MTF stays balanced

for considerable time period (0.5–1 h) prior to the sudden flux unloading, constituted a considerable part (a quarter) of all substorms observed by Geotail spacecraft. It was shown that the magnetic configuration, rather than the MTF value, is crucial for the substorm initiation.

4. Both GMHD and empirical Tsyganenko models do not allow to test the method tailward of 30 R_E. Recently, *Angelopoulos et al.* [2013] applied this method (with some modifications) to Advanced Relay And Technology Mission observations made at lunar orbit to compute the MTF variations during substorms. These computations provide a convincing evidence that energy dissipation at the earthward and tailward propagating dipolarization fronts significantlyl contribute to the global energy dissipation and to the magnetic flux transfer during substorms. Statistical adaptation and validation of the method for the cislunar magnetotail is an interesting task for future studies.

As this two-spacecraft method is currently the only direct method allowing to monitor the MTF variations in near real time as well as in retrospective, we look forward to foresee its interesting future applications in the studies of the global magnetospheric dynamics and magnetospheric modeling.

Acknowledgments

This work was supported by Russian Science Foundation grant 14-17-00072. The CLUSTER-based tail magnetic flux computation for years 2001–2009 was supported by FP7 ECLAT project, they are now available via CSA. We are grateful to all teams for the opportunity to use their observational data. We thank NASA CDAWeb (http://cdaweb.gsfc.nasa.gov/istp_public/) for IMF, solar wind, and magnetic index data; the AMPERE project (http://ampere.jhuapl.edu) for AMPERE data; the THEMIS website (http://themis.ssl.berkeley.edu/) for THEMIS spacecraft data, Cluster Science Archive (http://www.cosmos.esa.int/web/csa) for Cluster data; the IMAGE-FUV data were supplied by the NASA Space Science Data Centre(NSSDC). The global MHD simulations were made possible due to NASA Community Coordinated Modeling Center effort (http://ccmc.gsfc.nasa.gov/). S.E.M. was supported by the Science and Technology Facilities Council (STFC), UK, grant ST/K001000/1. The work at the Birkeland Centre for Space Centre, University of Bergen, Norway, was supported by the Research Council of Norway/CoE under contract 223252/F50. We also thank Stepan Dubyagin for help in calculating THEMIS total pressure, Peter Boakes for data on magnetotail plasma domains, and Marianna Kholeva for help with the manuscript preparation.

References

Anderson, B. J., K. Takahashi, and B. A. Toth (2000), Sensing global Birkeland currents with Iridium engineering magnetometer data, *Geophys. Res. Lett.*, *27*, 4045–4048, doi:10.1029/2000GL000094.

Anderson, B. J., K. Takahashi, T. Kamei, C. L. Waters, and B. A. Toth (2002), Birkeland current system key parameters derived from Iridium observations: Method and initial validation results, *J. Geophys. Res.*, *107*, SMP 11–1 – SMP 11-13, doi:10.1029/2001JA000080.

Angelopoulos, V., A. Runov, X.-Z. Zhou, D. L. Turner, S. A. Kiehas, S.-S. Li, and I. Shinohara (2013), Electromagnetic energy conversion at reconnection fronts, *Science*, *43*, 1478–1482.

Artemyev, A. V., A. A. Petrukovich, R. Nakamura, and L. M. Zelenyi (2015), Two-dimensional configuration of the magnetotail current sheet: THEMIS observations, *Geophys. Res. Lett.*, *42*, 3662–3667, doi:10.1002/2015GL063994.

Baker, D. N., et al. (1996), The neutral line model of substorms: Past results and present view, *J. Geophys. Res.*, *101*, 12,975–13,010.

Baumjohann, W., G. Paschmann, and T. Nagai (1992), Thinning and expansion of the substorm plasma sheet, *J. Geophys. Res.*, *97*, 17,173–17,175, doi:10.1029/92JA01519.

Boakes, P. D., S. E. Milan, G. A. Abel, M. P. Freeman, G. Chisham, B. Hubert, and T. Sotirelis (2008), On the use of IMAGE FUV for estimating the latitude of the open/closed magnetic field line boundary in the ionosphere, *Ann. Geophys.*, *26*, 2759–2769.

Boakes, P. D., S. E. Milan, G. A. Abel, M. P. Freeman, G. Chisham, and B. Hubert (2009), A statistical study of the open magnetic flux content of the magnetosphere at the time of substorm onset, *Geophys. Res. Lett.*, *36*, L04105, doi:10.1029/2008GL037059.

Boyle, C. B., P. H. Reiff, and M. R Harrison (1997), Empirical polar cap potentials, *J. Geophys. Res.*, *102*, 111–125.

Brittnacher, M., M. Fillingim, G. Parks, G. Germany, and J. Spann (1999), Polar cap area and boundary motion during substorms, *J. Geophys. Res.*, *104*, 12,251–12,262, doi:10.1029/1998JA900097.

Caan, M. N., R. L. McPherron, and C. T. Russell (1978), The statistical magnetic signature of magnetospheric substorms, *Planet. Space Sci.*, *26*, 269–279, doi:10.1016/0032-0633(78)90092-2.

Carter, J. A., S. E. Milan, J. C. Coxon, M.-T. Walach, and B. J. Anderson (2016), Average field-aligned current configuration parameterized by solar wind conditions, *J. Geophys. Res. Space Physics*, *121*, 1294–1307, doi:10.1002/2015JA021567.

Clausen, L. B. N., J. B. H. Baker, J. M. Ruohoniemi, S. E. Milan, and B. J. Anderson (2012), Dynamics of the region 1 Birkeland current oval derived from the Active Magnetosphere and Planetary Electrodynamics Response Experiment (AMPERE), *J. Geophys. Res.*, *117*, A06233, doi:10.1029/2012JA017666.

Clausen, L. B. N., J. B. H. Baker, J. M. Ruohoniemi, S. E. Milan, J. C. Coxon, S. Wing, S. Ohtani, and B. J. Anderson (2013), Temporal and spatial dynamics of the regions 1 and 2 Birkeland currents during substorms, *J. Geophys. Res. Space Physics*, *118*, 3007–3016, doi:10.1002/jgra.50288.

Coroniti, F. V., and C. F. Kennel (1972), Changes in magnetospheric configuration during the substorm growth phase, *J. Geophys. Res.*, *77*, 3361–3370.

Cowley, S. W. H., and M. Lockwood (1992), Excitation and decay of solar wind-driven flows in the magnetosphere-ionosphere system, *Ann. Geophys.*, *10*, 103–115.

DeJong, A., and C. Clauer (2005), Polar UVI images to study steady magnetospheric convection events: Initial results, *Geophys. Res. Lett.*, *32*, L24101, doi:10.1029/2005GL024498.

DeJong, A. D., et al. (2007), Aurora and open magnetic flux during isolated substorms, sawteeth, and SMC events, *Ann. Geophys.*, *25*, 1865–1876.

DeJong, A. D., A. J. Ridley, and C. R. Clauer (2008), Balanced reconnection intervals: Four case studies, *Ann. Geophys.*, *26*, 3897–3912.

Dewhurst, J. P., C. J. Owen, A. N. Fazakerley, and A. Balogh (2004), Thinning and expansion of the sub-storm plasma sheet: Cluster PEACE timing analysis, *Ann. Geophys.*, *22*, 4165–4184.

Dmitrieva, N. P., V. A. Sergeev, and M. A. Shukhtina (2004), Average characteristics of the midtail plasma sheet in different dynamic regimes of the magnetosphere, *Ann. Geophys.*, *22*, 2107–2113.

Dungey, J. W. (1961), Interplanetary magnetic fields and the auroral zones, *Phys. Rev. Lett.*, *6*, 47–48.

Fairfield, D. H. (1985), Solar wind control of magnetospheric pressure (CDAW 6), *J. Geophys. Res.*, *90*(A2), 1201–1204, doi:10.1029/JA090iA02p01201.

Freeman, M. P., and C. J. Farrugia (1999), Solar wind input between substorm onsets during and after the October 18–20, 1995, magnetic cloud, *J. Geophys. Res.*, *104*(A10), 22,729–22,744, doi:10.1029/1999JA900204.

Gordeev, E. I., V. A. Sergeev, T. I. Pulkkinen, and M. Palmroth (2011), Contribution of magnetotail reconnection to the cross-polar cap electric potential drop, *J. Geophys. Res.*, *116*, A08219, doi:10.1029/2011JA016609.

Gordeev, E. I., V. A. Sergeev, I. Honkonen, M. Kuznetsova, L. Rastätter, M. Palmroth, P. Janhunen, G. Toth, J. Lyon, and M. Wiltberger (2015), Assessing the performance of community-available global MHD models using key system parameters and empirical relationships, *Space Weather*, *13*, 868–884, doi:10.1002/2015SW001307.

Huang, C.-S., A. D. DeJong, and X. Cai (2009), Magnetic flux in the magnetotail and polar cap during sawteeth, isolated substorms, and steady magnetospheric convection events, *J. Geophys. Res.*, *114*, A07202, doi:10.1029/2009JA014232.
Hubert, B., S. E. Milan, A. Grocott, S. W. H. Cowley, and J.-C. Gérard (2006), Dayside and nightside reconnection rates inferred from IMAGE FUV and SuperDARN data, *J. Geophys. Res.*, *111*, A03217, doi:10.1029/2005JA011140.
Janhunen, P., M. Palmroth, T. V. Laitinen, I. Honkonen, L. Juusola, G. Facskó, and T. I. Pulkkinen (2012), The GUMICS-4 global MHD magnetosphere–ionosphere coupling simulation, *J. Atmos. Sol. Terr. Phys.*, *80*, 48–59, doi:10.1016/j.jastp.2012.03.006.
Lin, R. L., X. X. Zhang, S. Q. Liu, Y. L. Wang, and J. C. Gong (2010), A three-dimensional asymmetric magnetopause model, *J. Geophys. Res.*, *115*, A04207, doi:10.1029/2009JA014235.
Lyons, L. R. (1998), The geospace modeling program grand challenge, *J. Geophys. Res.*, *103*, 14,781–14,785, doi:10.1029/98JA00015.
Lyon, J. G., J. A. Fedder, and C. M. Mobarry (2004), The Lyon–Fedder–Mobarry (LFM) global MHD magnetospheric simulation code, *J. Atmos. Sol. Terr. Phys.*, *66*, 1333–1350.
Maezawa, K. (1975), Magnetotail boundary motion associated with geomagneticsubstorms, *J. Geophys. Res.*, *80*, 3543–3548, doi:10.1029/JA080i025p03543.
Milan, S. E., M. Lester, S. W. H. Cowley, K. Oksavik, M. Brittnacher, R. A. Greenwald, G. Sofko, and J.-P. Villain (2003), Variations in the polar cap area during two substorm cycles, *Ann. Geophys.*, *21*, 1121–1140, doi:10.5194/angeo-21-1121-2003.
Milan, S. E., G. Provan, and B. Hubert (2007), Magnetic flux transport in the Dungey cycle: A survey of dayside and night-side reconnection rates, *J. Geophys. Res.*, *112*, A01209, doi:10.1029/2006JA011642.
Milan, S. E., P. D. Boakes, and B. Hubert (2008), Response of the expanding/contracting polar cap to weak and strong solar wind driving: Implications for substorm onset, *J. Geophys. Res.*, *113*, A09215, doi:10.1029/2008JA013340.
Mishin, V. M. (1990), The magnetogram inversion technique and some applications, *Space Sci. Rev.*, *53*, 83–163, doi:10.1007/BF00217429.
Miyashita, Y., et al. (2009), A state-of-the-art picture of substorm-associated evolution of the near-Earth magnetotail obtained from superposed epoch analysis, *J. Geophys. Res.*, *114*, A01211, doi:10.1029/2008JA013225.
Panov, E. V., et al. (2010), Plasma sheet thickness during a bursty bulk flow reversal, *J. Geophys. Res.*, *115*, A05213, doi:10.1029/2009JA014743.
Palmroth, M., T. I. Pulkkinen, P. Janhunen, and C.-C. Wu (2003), Stormtime energy transfer in global MHD simulation, *J. Geophys. Res.*, *108*, A11048, doi:10.1029/2002JA009446.
Petrinec, S. M., and C. T. Russell (1996), Near-Earth magnetotail shape and size as determined from the magnetopause flaring angle, *J. Geophys. Res.*, *101*, 137–152, doi:10.1029/95JA02834.
Petrukovich, A. A., W. Baumjohann, R. Nakamura, A. Runov, A. Balogh, and H. Reme (2007), Thinning and stretching of the plasma sheet, *J. Geophys. Res.*, *112*, A10213, doi:10.1029/2007JA012349.
Petrukovich, A. A., A. V. Artemyev, H. V. Malova, V. Y. Popov, R. Nakamura, and L. M. Zelenyi (2011), Embedded current sheets in the Earth's magnetotail, *J. Geophys. Res.*, *116*, A00I25, doi:10.1029/2010JA015749.
Powell, K. G., P. L. Roe, T. J. Linde, T. I. Gombosi, and D. L. de Zeeuw (1999), A solution-adaptive upwind scheme for ideal magnetohydrodynamics, *J. Comput.Phys.*, *154*, 284–309, doi:10.1006/jcph.1999.6299.
Raeder, J. (2003), *Global Magnetohydrodynamics—Tutorial, in Space Plasma Simulation*, edited by J. Büchner, C.T. Dum, and M. Scholer, Springer, Berlin.
Raeder, J., D. Larson, W. Li, L. Kepko, and T. Fuller-Rowell (2008), OpenGGCM simulations for the THEMIS mission, *Space Sci. Rev.*, *141*(1–4), 535–555, doi:10.1007/s11214-008-9421-5.
Rong, Z. J., W. X. Wan, C. Shen, X. Li, M. W. Dunlop, A. A. Petrukovich, T. L. Zhang, and E. Lucek (2011), Statistical survey on the magnetic structure in magnetotail current sheets, *J. Geophys. Res.*, *116*, A09218, doi:10.1029/2011JA016489.
Runov, A., et al. (2005), Electric current and magnetic geometry in flappingmagnetotail current sheets, *Ann. Geophys.*, *23*, 1391–1403.
Russell, C. T., and R. L. McPherron (1973), The magnetotail and substorms, *Space Sci. Rev.*, *15*, 205–266, doi:10.1007/BF00169321.
Sergeev, V. A., and T. Bösinger (1993), Particle dispersion at the nightside boundary of the polar cap, *J. Geophys. Res.*, *98*, 233–241.
Sergeev, V. A., D. G. Mitchell, C. T. Russell, and D. J. Williams (1993), Structure of the tail plasma/current sheet at 11 R_E and its changes in the course of a substorm, *J. Geophys. Res.*, *98*, 17,345–17,366, doi:10.1029/93JA01151.
Sergeev, V. A., R. J. Pellinen, and T. I. Pulkkinen (1996), Steady magnetospheric convection: A review of recent results, *Space Sci. Rev.*, *75*(3–4), 551–604.
Sergeev, V. A., V. Angelopoulos, C. Carlson, and P. Sutcliffe (1998), Current sheet measurements within a flapping plasma sheet, *J. Geophys. Res.*, *103*, 9177–9187.
Sergeev, V., et al. (2003), Current sheet flapping motion and structure observed by Cluster, *Geophys. Res. Lett.*, *30*, 1327, doi:10.1029/2002GL016500.
Shukhtina, M. A., and E. Gordeev (2015), In situ magnetotail magnetic flux calculation, *Ann. Geophys.*, *33*, 769–781.
Shukhtina, M. A., N. P. Dmitrieva, and V. A. Sergeev (2004), Quantitative magnetotail characteristics of different magnetospheric states, *Ann. Geophys.*, *22*, 1019–1032.
Shukhtina, M. A., et al. (2005), Observational evidence of the loading-unloading substorm scheme, *Geophys. Res. Lett.*, *32*, L17107, doi:10.1029/2005GL023779.
Shukhtina, M. A., E. I. Gordeev, and V. A. Sergeev (2009), Time-varying magnetotail magnetic flux calculation: A test of the method, *Ann. Geophys.*, *27*, 1583–1591.
Shukhtina, M. A., et al. (2010), Comparison of magnetotail magnetic flux estimates based on global auroral images and simultaneous solar wind-magnetotail measurements, *J. Atmosph. Sol. Terr. Phys.*, *72*, 1282–1291.
Shukhtina, M. A., N. P. Dmitrieva, and V. A. Sergeev (2014), On the conditions preceding sudden magnetotail magnetic flux unloading, *Geophys. Res. Lett.*, *41*, 1093–1099, doi:10.1002/2014GL059290.
Siscoe, G. L., and T. S. Huang (1985), Polar cap inflation and deflation, *J. Geophys. Res.*, *90*, 543–547.
Spreiter, J. R., A. Y. Alksne, and A. L. Summers (1966), Hydromagnetic flow around the magnetosphere, *Planet. Space Sci.*, *14*, 223–248.
Tanskanen, E. I., et al. (2005), Magnetotail response to prolonged southward IMF B_z intervals: Loading, unloading, and continuous magnetospheric dissipation, *J. Geophys. Res.*, *110*, A03216, doi:10.1029/2004JA010561.
Thompson, S. M., M. G. Kivelson, K. K. Khurana, R. L. McPherron, J. M. Weygand, A. Balogh, H. Réme, and L. M. Kistler (2005), Dynamic Harris current sheet thickness from Cluster current density and plasma measurements, *J. Geophys. Res.*, *110*, A02212, doi:10.1029/2004JA010714.
Tsyganenko, N. A., and D. H. Fairfield (2004), Global shape of the magnetotail current sheet as derived from Geotail and Polar data, *J. Geophys. Res.*, *109*, A03218, doi:10.1029/2003JA010062.
Tsyganenko, N. A. (2014), Data-based modeling of the geomagnetosphere with an IMF-dependent magnetopause, *J. Geophys. Res. Space Physics*, *119*, 335–354, doi:10.1002/2013JA019346.

Tsyganenko, N. A., and V. A. Andreeva (2015), A forecasting model of the magnetosphere driven by an optimal solar wind coupling function, *J. Geophys. Res. Space Physics*, *120*, 8401–8425, doi:10.1002/2015JA021641.

Yahnin, A. G., et al. (1994), *Development of the Substorm Ending the Steady Magnetospheric Convection Interval*, Proceedings of ICS-2, Fairbanks, Alaska, USA.

Walsh A. P., et al. (2014), Dawn–dusk asymmetries in the coupled solar wind–magnetosphere–ionosphere system: A review, *Ann. Geophys.*, *32*, 705–737.

Yahnin, A. G., et al. (2001), Correlated Interball/ground-based observations of isolated substorm: The pseudobreakup phase, *Ann. Geophys.*, *19*, 687–698.

Zhang, Y., L. J. Paxton, and H. Kil (2011), Nightside polar rain aurora boundary gap and its applications for magnetotail reconnection, *J. Geophys. Res.*, *116*, A11214, doi:10.1029/2011JA016884.